Dalton Transactions

An international journal of inorganic chemistry

Accepted Manuscript

This article can be cited before page numbers have been issued, to do this please use: M. F. Mohamad Noh, H. Ullah, N. A. Arzaee, A. bin Ab Halim, M. A. F. Abdul Rahim, N. A. Mohamed, J. Safaei, S. N. F. Mohd Nasir, G. Wang and M. A. Mat Teridi, *Dalton Trans.*, 2020, DOI: 10.1039/D0DT00406E.

ROYAL SOCIETY OF CHEMISTRY

rsc.li/dalton

View Article Online
DOI: 10.1039/D0DT00406E

ARTICLE

Rapid Fabrication of Oxygen Defective α-Fe_2O_3(110) for Enhanced Photoelectrochemical Activities

Received 00th January 20xx,
Accepted 00th January 20xx

DOI: 10.1039/x0xx00000x

Mohamad Firdaus Mohamad Noh,*[a] Habib Ullah,*[b] Nurul Affiqah Arzaee,[a] Azhar Ab Halim,[a,c] Muhammad Amir Faizal Abdul Rahim,[a,c] Nurul Aida Mohamed,[a] Javad Safaei,[d] Siti Nur Farhana Mohd Nasir,[a] Guoxiu Wang,[d] Mohd Asri Mat Teridi*[a]

Defect engineering is increasingly recognized as a viable strategy for boosting the performance of photoelectrochemical (PEC) water splitting by metal oxide-based photoelectrodes. However, previously developed methods for generating point defect associated with oxygen vacancies is rather time-consuming. Herein, high density oxygen deficient α-Fe_2O_3 with dominant (110) crystal plane is developed in very short timescale of 10 minutes by employing aerosol-assisted chemical vapor deposition and pure nitrogen as gas carrier. The oxygen defective film exhibits almost 8 times higher photocurrent density compared to hematite photoanode with low concentration of oxygen vacancies which is prepared in purified air. The existence of oxygen vacancies improves light absorption ability, accelerates charge transport in the bulk of film, and promotes charge separation at electrolyte/semiconductor interface. DFT simulations verify that oxygen defective hematite has a narrow band gap, electron-hole trapped centre, and strong adsorption energy of water molecules compared to that of pristine hematite. This strategy might bring PEC technology another step further towards large-scale fabrication for future commercialization.

Introduction

Solar energy is expected to be the primary source for driving future growth as it is eco-friendly, safe, abundant and unlimited. The intermittent nature of solar energy makes energy storage essential for providing continuous energy supply to the electricity grid.[1] One of the most excellent ideas for storing solar energy is to use excess energy from sunlight and split water into its constituents such as hydrogen and oxygen. The hydrogen acts as an energy storage medium, where it could be converted to electricity at times of supply shortage via green route with the only by-products being water.[2,3] Photoelectrochemical (PEC) water splitting with the aid of semiconductor is one of the promising technology in producing high-purity hydrogen. To date, numerous materials such as TiO_2,[4] SnO_2,[5,6] $BiVO_4$[7,8] and g-C_3N_4[9,10] have been explored as photoanode for the PEC water splitting.

Another promising material which exhibits positive potential for generating hydrogen by means of PEC process is the alpha phase of iron oxide (α-Fe_2O_3) or so-called hematite. Among other known phases of iron oxide such as beta (*β*) and gamma (*γ*) phases, crystalline iron oxide typically appears in the form of α-Fe_2O_3. The reason behind this is it's thermodynamic stability at ambient conditions.[11,12] In addition, hematite possesses non-toxic property, widespread availability, low cost, and suitable band gap energy (2.0-2.2 eV), rendering it suitable for photoanode in large-scale PEC systems.[12–14] Theoretically, hematite is capable of achieving solar-to-hydrogen (STH) efficiency up to 16.8% under 1 Sun irradiation (100 mW/cm^2, 1.5 G illumination) at 1.23 $V_{RHE.}$[15,16] The theoretical value exceeds the STH benchmark efficiency for practical application which is 10%.[3,12] However, the performance of PEC water splitting based on state-of-the-art hematite photoanode is still far below the target. This is attributed to the challenging task to balance the extremely short hole diffusion length (about 2-4 nm) and the long absorption depth of photons of hematite, to obtain efficient charge extraction and high-light absorption.[17,18]

Lots of efforts have been devoted to enhance the PEC performance of hematite photoanode including modification of nanostructures,[19,20] introduction of dopant,[21,22] coupling with other semiconductor to form composite[23] or heterojunction devices[24] and creation of point defects associated with oxygen vacancies.[25,26] From the viewpoint of oxygen vacancies, several research groups have observed considerable improvement in PEC performance of hematite thin films, since oxygen vacancies can serve as electron donors to ameliorate bulk conductivity and facilitate charge separation.[27] Besides, oxygen vacancies

[a] Solar Energy Research Institute, Universiti Kebangsaan Malaysia, 43600 Bangi, Selangor, Malaysia.
[b] Renewable Energy Group, College of Engineering, Mathematics and Physical Sciences, University of Exeter, Penryn Campus, Cornwall, TR10 9FE, United Kingdom.
[c] School of Applied Physics, Faculty of Science and Technology, Universiti Kebangsaan Malaysia, 43600 Bangi, Selangor, Malaysia.
[d] Centre for Clean Energy Technology, School of Mathematical and Physical Sciences, University of Technology Sydney, Sydney, NSW 2007, Australia.
Email: fir.noh@gmail.com (M.F.M. Noh); hu203@exeter.ac.uk (H. Ullah); asri@ukm.edu.my (M.A.M. Teridi)
Electronic Supplementary Information (ESI) available: Crystallite size calculation, transient time calculation, I-t curve, reproducibility, AFM and FESEM images. See DOI: 10.1039/x0xx00000x

would also modify the surface component which is favorable for water adsorption and subsequently enhance surface catalytic activity.[16,28] Nevertheless, the processing techniques developed to introduce oxygen defects in hematite thin films currently are time-consuming and irrelevant for large-scale production. This is due to the fact that most reports employed additional treatment towards the pre-fabricated hematite film to generate the defect sites. For instance, Zhao *et al*.[27] reported a 20 min method for the preparation of compact hematite film, using metal-organic decomposition method, annealed under N_2 flow for 2 hours to form oxygen deficient sample. Wang *et al*.[25] applied a double-step thermal oxidation/reduction process on iron foils where the foils were initially annealed in air followed by annealing in Ar atmosphere. The whole fabrication process needed more than 3 hours to produce hematite nanorods with oxygen vacancies. Other approach of making oxygen vacancies in hematite includes plasma treatment of pre-sintered hematite nanoflakes, which need at least 25 min.[16]

To overcome the extensive time consumption of the defective hematite film fabrication, additional processing protocols should be eliminated. Therefore, a technique to simultaneously introduce oxygen vacancies during the fabrication process of hematite layer must be developed. For that purpose, one of the practicable strategies is to adopt aerosol-assisted chemical vapor deposition (AACVD) method. AACVD is basically a variant of the well-established chemical vapor deposition (CVD) technique for the deposition of thin films. However, in case of AACVD process, an external atomic transducer can be used to vaporize the liquid solution, containing the precursors which negates the reliance on the volatility of precursor, widens the choice of precursor, and minimizes the power consumption.[5,29] Moreover, AACVD enables facile control of the morphological and structural properties of the thin film by manipulating the deposition parameters such as deposition time, precursor concentration, and type of carrier gas which in turn affects their electrical and optical properties.[5] Numerous photoelectrodes with impressive performance have been developed using this technique including TiO_2,[30] Fe_2O_3,[31] $BiVO_4$[32] and NiO[33] which prove its excellent performance to be used in commercial applications.

Previously, we have successfully demonstrated AACVD process with purified air as gas carrier, applicable for eliminating oxygen vacancies in SnO_2 thin film which is advantageous for perovskite solar cells device but detrimental towards the PEC water splitting.[34] In this work, oxygen vacancies are intentionally generated in Fe_2O_3 film by introducing nitrogen environment in fabrication process of photoanode via AACVD process, to boost the overall PEC performance. Photocurrent density of this sample have been found to be eightfold compared to that of purified air flow which contains less oxygen defects. Such phenomenon was primarily attributed to the magnificent optical and electrical properties which is elaborated in details in this study. The thickness of the films was also tuned by regulating the deposition period to understand the superior ability of oxygen vacancies in enhancing the PEC performance of Fe_2O_3. It is found that the duration of optimum device fabrication is only 10 min which is the fastest ever-reported fabrication of defective hematite photoanode. Furthermore, this signify the great potential of this approach for further development. Finally, periodic density functional theory (DFT) simulations were carried out to countercheck the experimental data. We have constructed different surfaces of hematite, however the 110 surface matches our experimental thin film, and is more stable so, the calculations are restricted to this phase. It is found that defective hematite has high adsorption energy towards water molecules, electron-hole trapping centers in Fermi level, and narrow band gap compared to that of pristine. In summary, an excellent correlation between theory and experiments is found which validate and confirm the main idea of this work.

Experimental

Materials

Fluorine-doped tin oxide (FTO) glass (Pilkington, sheet resistance of 15 Ω sq^{-1}) was employed as substrate. Iron chloride hexahydrate ($FeCl_3.6H_2O$, 97%) and sodium sulfate (Na_2SO_4, 99%) were purchased from Sigma Aldrich. Absolute ethanol and acetone was obtained from VWR International Limited and R&M Chemicals, respectively. Deionized (DI) water purified at 18 MΩ was acquired from Thermal Scientific Barnstead Smart2 Pure water purification system.

Fabrication of Fe_2O_3 thin film

0.1 M precursor solution was made by dissolving $FeCl_3.6H_2O$ in absolute ethanol and stirred vigorously for 30 min at room temperature. The solution was left overnight before use. FTO substrates (2cm × 1cm) were cleaned ultrasonically with ethanol, acetone, and DI water for 10 min sequentially, followed by drying under nitrogen flow. Deposition of Fe_2O_3 film was conducted through a homemade AACVD system, as reported in our previous report.[20] In brief, approximately 20 mL of the precursor was inserted in the precursor container. A commercial humidifier was utilized to atomize the precursor at full power to create saturated vapor in the container. The vapor of precursor was transported to another container (filtration chamber), using purified air at a rate of 280 cm^3 min^{-1} and simultaneously, additional purified air of 1530 cm^3 min^{-1} was supplied into the same container to reduce the concentration of the vapor. Afterwards, the gas mixture was directed to a hot reaction chamber containing a pre-cleaned substrate placed on 450 ˚C hot plate. The deposition was performed for 10 minutes. Finally, a similar process has been employed for pure nitrogen gas supply.

Characterization

X-ray diffraction (XRD) was carried out using X-ray diffractometer (Bruker, D8 Advance, Cu Kα radiation, λ = 154.18 pm, 2θ = 20-80˚) to analyse the crystal structure of Fe_2O_3 thin film. The thickness of the film was determined with a profilometer (Dektak XT, Bruker). Nanosurf Easyscan2 atomic

View Article Online
DOI: 10.1039/D0DT01965

force microscopy (AFM) was employed to study the roughness of samples. The morphology of films was analyzed by ZEISS Merlin field emission scanning electron microscopy (FESEM). Transmission electron microscopy (TEM) images were taken using Thermo Fisher, Talos 120C. The elemental composition and types of chemical bond were investigated using Auger Electron Spectroscopy with X-Ray Photoelectron Spectrometer (XPS), Axis Ultra Kratos/Shimadzu. Lambda 35 Perkin Elmer UV visible spectrophotometer was utilized for determining the optical properties. The performance of photoanode with an active area of 1.0 cm^2 was determined using chronoamperometry, linear sweep voltammetry (LSV) and electrochemical impedance spectroscopy (EIS). For this purpose, Metrohm Autolab electrochemical workstation under simulated one sun illumination and dark condition including three electrodes configuration were employed. The prepared samples were used as working electrode while Pt as counter electrode and Ag/AgCl as reference electrode. The electrodes were immersed in 0.5M Na_2SO_4 aqueous solution. During LSV measurement, the voltage was swept from 0 V to 1.7 $V_{Ag/AgCl}$ at a scan rate of 100 mV s^{-1}. The following Nernst equation was applied to convert the experimentally measured potentials *versus* Ag/AgCl ($E_{Ag/AgCl}$) to the potentials *versus* reversible hydrogen electrode (E_{RHE}).

$$E_{\mathrm{RHE}} = E_{\mathrm{Ag/AgCl}} + E^{0}_{\mathrm{Ag/AgCl}} + 0.059\ \mathrm{pH}\ (1)$$

where $E^0_{Ag/AgCl}$ = 0.209 V at 25 °C for a Ag/AgCl electrode in 3 M NaCl and pH = 7.0 for the electrolytes based on 0.5M Na_2SO_4.[7] The stability of the sample was also measured using chronoamperometry for 30 min under bias voltage of 1.2 $V_{Ag/AgCl}$. During EIS measurements, a frequency of 10^5 to 0.1 Hz and bias voltage of 1.2 $V_{Ag/AgCl}$ was applied. Mott-Schottky analysis was performed under dark condition at 1000 Hz, 2000 Hz and 3000 Hz. High frequency was chosen to prevent the filling/unfilling of surface states or the buildup of a double-layer capacitance. Furthermore, different frequencies are necessary to evaluate the possible frequency dispersion.

Computational Methodology

Density functional theory (DFT) calculations are performed on Quantum-ATK[35] and the results are visualized on VESTA and Virtual NanoLab Version 2019.3.[36] In order to model the Fe_2O_3(110) and its oxygen defective surface, primitive unit cell with space group of R3c, lattice parameters of *a*=*b*=c=5.21Å and α=β=γ=54.55°, is taken as unit cell. The linear combination of atomic orbitals (LCAO) method has been used for the Fe and O atoms[37] where different pseudopotentials are employed to reproduce the experimental band gap. Recently, a band gap of 1.53 eV has been reported for alpha hematite,[38] using GGA+U method. However, this 1.53 eV band gap is still underestimated to that of experimental one. In this work, we used spin polarized exchange correlation functional along with Hubbard model. Different Hubbard parameters are employed, where the (U-J) value of 5.5 eV is selected for Fe. In order to fit the experimental data, these high (U-J) values are required.[39] After optimizing the lattice parameters of the bulk unit cell; a supercell (2x2x2) is constructed, from which (110) surface is built. The thickness of the slab is kept as enough as that of eight unit cells and a vacuum of 10Å is created. Stability of this surface is confirmed from the positive surface formation energy, followed by oxygen defective surface, O_v_Fe_2O_3(110). The surface formation energies of these slabs are estimated using our previously reported method.[7,40,41] Generalized gradient approximation (GGA) with the Perdew-Burke-Ernzerhof (PBE) exchange-correlation functional and pseudopotential of Hartwigsen Goedecker-Hutter (HGH) with tier 4 basis utilized for the structural and energy optimization.[42] A 5x5x5 Monkhorst-Pack k-grid with an energy cut-off of 700 eV is used for the unit cell, while a 5x5x1 k-point mesh is used for Fe_2O_3(110) and O_v_Fe_2O_3(110) surfaces. The density of states (DOS), partial density of states (PDOS), band structure, effective potential, electron density difference (EDD) and electron localization functional (ELF) are also simulated.

Results and Discussion

Experimental Results

As discussed earlier, hematite layer was fabricated via AACVD system using different carrier gas, namely purified air and pure nitrogen, where the former represents excess oxygen environment while the latter indicates inadequate oxygen environment. All these conditions were operated for 10 min to ensure similar thickness of both samples. Fe_2O_3 and O_v_Fe_2O_3 notations will be used to denote samples prepared under purified air and pure nitrogen flow, respectively. The thickness of both samples was approximately 350 nm as identified by profilometer indicating similar growth rate of hematite film regardless of the carrier gas employed. From FESEM images in Fig. 1, it can be seen that the surface of FTO is fully covered with hematite insinuating that AACVD technique enables homogenous deposition of metal oxide layer throughout the substrate.

The oxygen rich environment caused the Fe_2O_3 film to grow vertically and forms flakes-like nanostructure. Furthermore, due to the random orientation and thin size of the nanoflakes, the film has more porous domain and slightly exposes the FTO surface. On the other hand, the O_v_Fe_2O_3 samples exhibited irregular shard-like nanostructure which tend to agglomerate into bulky form with micro-scale size. The development of these nanostructures is closely related to the growing direction of the hematite crystal and will be discussed later. The 3-dimensional view of the as-prepared films are shown in AFM images (Fig. 1 (c) and (f)) where the root-mean-square (RMS) roughness for Fe_2O_3 and O_v_Fe_2O_3 were estimated to be 54.2 nm and 49.5 nm, respectively. The rougher surface of the former sample originates from the existence of deep porous region and sharp nanoflakes in Fe_2O_3 film.

The XRD measurement has been performed to investigate the crystallinity of the deposited thin films (Fig. 2), where the observable characteristic peaks of both samples can be indexed to the rhombohedral crystal structure of α-Fe_2O_3 or so-called

View Article Online
DOI: 10.1039/D0DT00406E

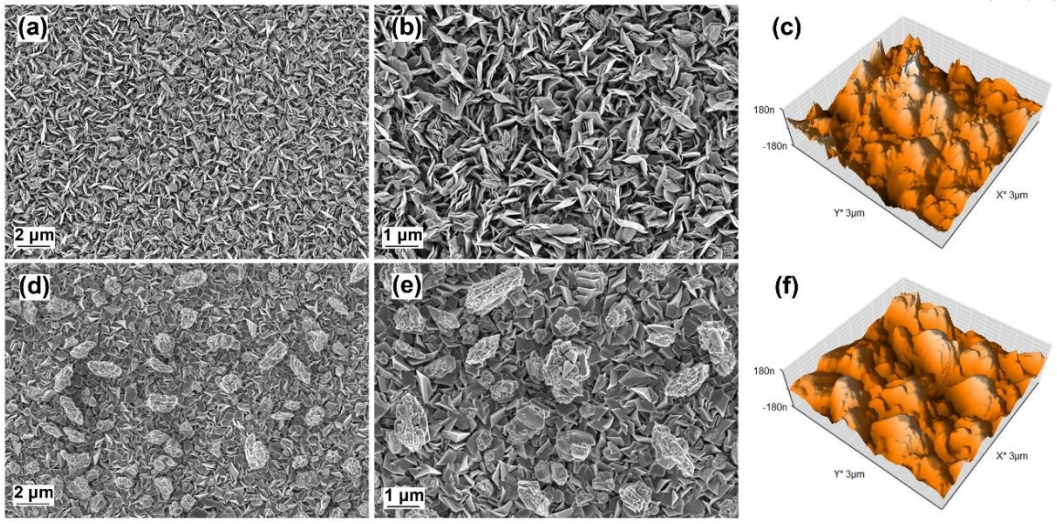

Fig. 1 FESEM images of (a-b) Fe_2O_3 and (d-e) O_v_Fe_2O_3 films viewed from top at different magnification scales. 3-D view of surface topography of (c) Fe_2O_3 and (f) O_v_Fe_2O_3 acquired from AFM analysis.

hematite (JCPDS No. 33-0664). Even though the O_v_Fe_2O_3 sample was fabricated under pure nitrogen flow, it should be noted that source of oxygen still exist in solution in the form of solvent and dissolved oxygen molecules which allows the conversion of Fe-based precursor to hematite. Moreover, other characteristic peaks corresponding to magnetite or other phases of iron oxide which typically appear during the fabrication of the film in oxygen deficient environment are not observable, implying that the energy supplied in AACVD technique is sufficient for complete reaction and crystal formation of hematite. Nonetheless, several peaks belong to FTO substrate are noticeable particularly for the Fe_2O_3 film due to the thin layer and the presence of porous domain which lead to incomplete surface coverage of Fe_2O_3 as described earlier. In addition, peak magnitude of (110) crystal plane is dominant for both samples but the intensity of this peak for Fe_2O_3 is greater than that of O_v_Fe_2O_3, signifying the improvement of crystallinity and formation of larger crystallite size. From hereafter, the Fe_2O_3 and O_v_Fe_2O_3 will be denoted as Fe_2O_3(110) and O_v_Fe_2O_3(110), respectively. With the aid of Scherrer equation (see Supporting Information), the average crystallite size of Fe_2O_3(110) and O_v_Fe_2O_3(110) were determined to be 106.25 nm and 42.49 nm, respectively. XRD pattern of O_v_Fe_2O_3(110) also shows a much higher ratio of peak intensity of (110) planes to peak intensity of other planes. Meanwhile, the peak intensity of crystal planes other than (110) plane increased for O_v_Fe_2O_3(110) sample. Oxygen deficient environment that was created by pure nitrogen gas carrier causes α-Fe_2O_3 to grow in multiple direction which explain the origin of shard-like shapes in O_v_Fe_2O_3(110) thin film.

The density of oxygen vacancies in Fe_2O_3(110) and O_v_Fe_2O_3(110) films was analyzed using XPS. Based on the high-resolution Fe 2p spectra in Fig. 2(b), three peaks corresponding to Fe $2p_{3/2}$, Fe $2p_{1/2}$ and Fe^{2+} satellite peak can be clearly observed at binding energy of 710.5 eV, 724.3 eV and 719.0 eV, respectively. These values are consistent with the binding energies typically reported for hematite.[43–45] The difference of Fe 2p spectra between Fe_2O_3(110) and O_v_Fe_2O_3(110) films is negligible. On the other hand, significant changes are detected for O 1s spectra of both samples as displayed in Fig. 2(c). The peak with low binding energy is associated with the oxygen in

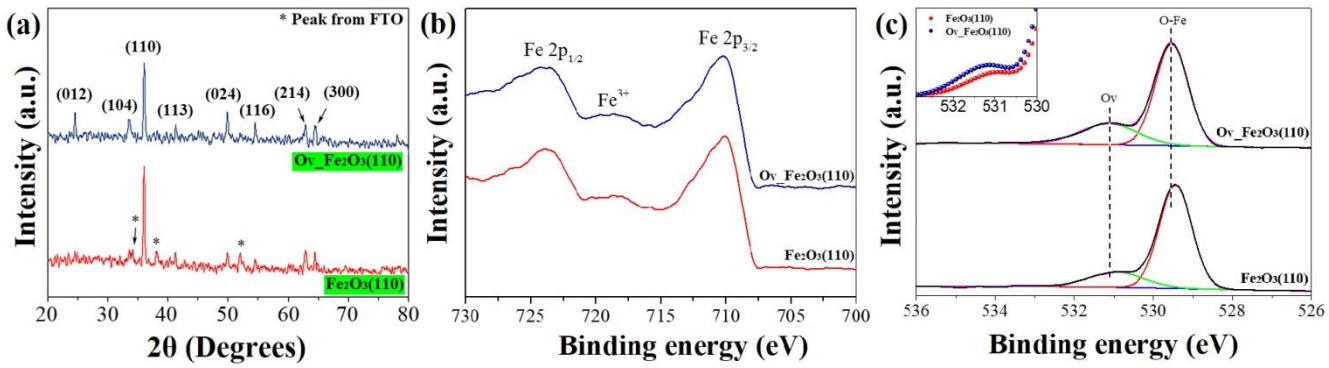

Fig. 2 (a) X-ray diffraction patterns of Fe_2O_3(110) and O_v_Fe_2O_3(110) film fabricated using AACVD. XPS spectra of (b) Fe 2p and (c) O 1s of the respective films. Inset of (c) shows the overlapping of O_v characteristic peak of both samples.

View Article Online
DOI: 10.1039/D0DT00406E

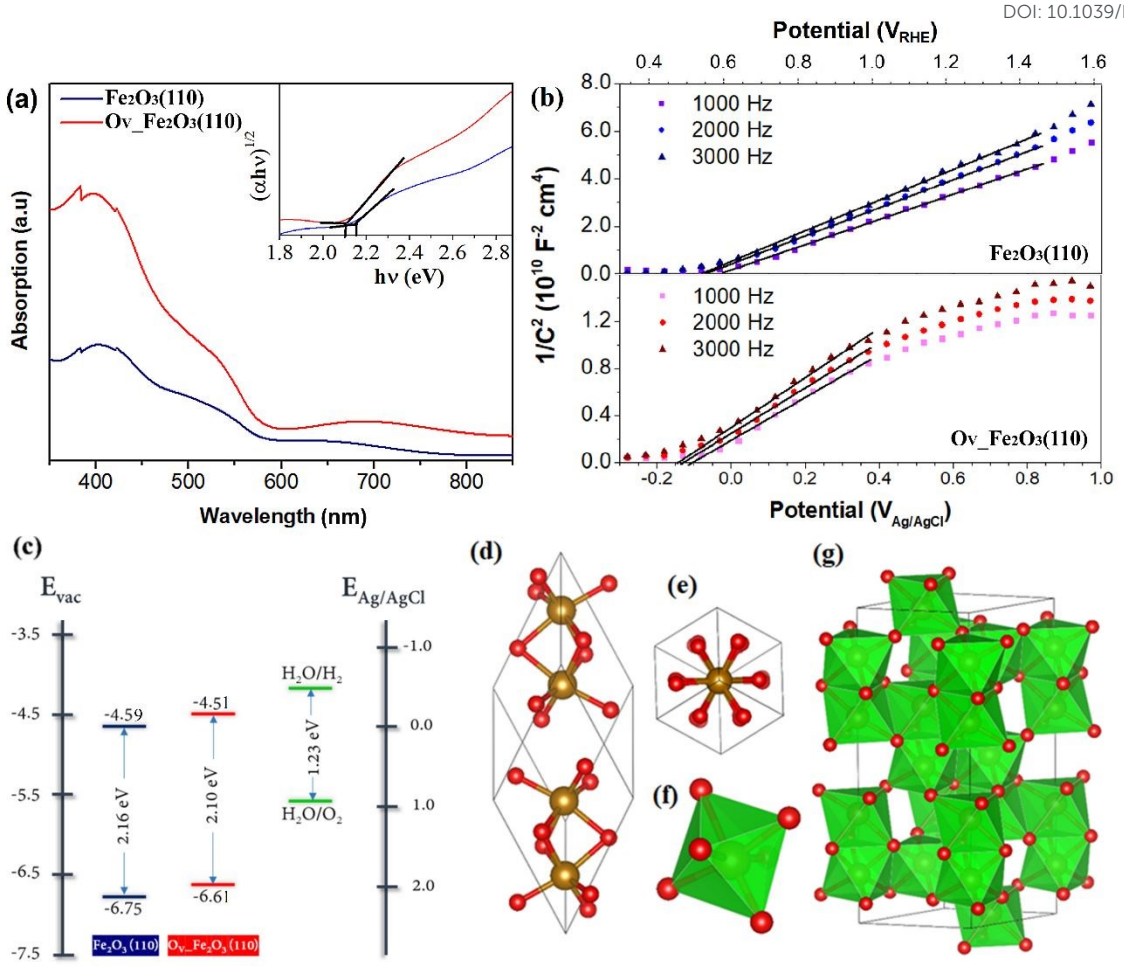

Fig. 3 (a) Absorbance spectra, (b) Mott-Schottky plot and (c) band diagram of Fe_2O_3(110) and O_v_Fe_2O_3(110) thin films. Inset of (a) is Tauc plot for determining their respective band gap. (d) Crystal structures of primitive unit cell of Fe_2O_3 (e) along with side view, (f) hexahedral geometry and (g) hexagonal bulk unit cell of Fe_2O_3.

the hematite lattice (O-Fe) whereas the peak at higher binding energy is related to the oxygen vacancies (O_v).[46] Apparently, the O-Fe and O_v peaks of the O_v_Fe_2O_3(110) sample shifted slightly to higher binding energy with respect to that of the Fe_2O_3(110) sample. This is because oxygen vacancies change the coordination of O atoms and chemical valence of Fe atoms which influences the O-Fe lattice and enhance the binding energy.[45,46] Besides, the magnitude of O_v characteristic peak of the O_v_Fe_2O_3(110) film is greater than that of the Fe_2O_3(110) counterpart as presented in the inset of Fig. 2(c). This proves that the deposition of hematite using AACVD under N_2 environment can amplify the density of oxygen vacancies. XPS survey spectra were also taken as represented in Fig. S1. Based on this spectra, other unwanted element such as Sn (which may appear due to the uncontrollable diffusion from FTO)[45,47] is not detected for both samples.

TEM images were also taken to examine the structural properties of the prepared samples at atomic level. Fig. S2(a-b) shows parallel fringes with lattice spacing of 0.25 nm, which can be assigned to the (110) plane of hematite.[48,49] Point defects associated with oxygen vacancies can also be clearly seen in the crystal lattice of O_v_Fe_2O_3(110) sample.

Light absorption property of hematite films was evaluated using UV-Vis spectroscopy (Fig. 3(a)). The light absorption onset for Fe_2O_3(110) thin film starts at approximately 574 nm corresponding to a band gap of 2.16 eV as deduced from the Tauc plot (inset of Fig. 3(a)) which is in line with the value reported in the literature.[50,51] Slight absorption tail that extends up to 770 nm is also visible for this sample. When the hematite film was deposited in nitrogen environment, substantial increment in light absorption across the entire spectral range was detected and the estimated band gap energy narrows to 2.10 eV in comparison to the film fabricated under purified air flow. This could be attributed to (i) the shard-like nanostructure that is well distributed throughout the surface of substrate forming a compact layer and (ii) the high density of defects related to oxygen vacancies in the crystal lattice and on the surface of O_v_Fe_2O_3(110) film. In terms of morphology, the compact thin film of O_v_Fe_2O_3(110) causes the incident light to be absorbed at each point on the substrate. On the other hand, Fe_2O_3(110) sample, which has exposed FTO surface as confirmed from XRD and FESEM analysis, allows part of the light to simply pass through it and reduces the light absorption capability. Meanwhile, the high concentration of oxygen

vacancies in O_v_Fe_2O_3(110) may induce the formation of new electronic states. Recently, it has been reported that shallow states at both band edges (i.e. electronic states near conduction band and valence band) of hematite and a deep donor state (i.e. deep electronic state near the valence band side) appear in the presence of oxygen vacancies.[52,53] This facilitates the photoexcitation of charge carriers by low energy photons and inhibits rapid charge recombination.[34] Moreover, the additional absorption tail becomes more apparent for O_v_Fe_2O_3(110) sample which can be ascribed as Urbach tail, formed by defective states in hematite.[54]

Fig. 3(b) displays Mott-Schottky plot of Fe_2O_3(110) and O_v_Fe_2O_3(110) photoanodes for three different frequencies measured in dark condition. A straight tangent line was built to help acquiring qualitative information about the charge transport properties of the samples. The apparent positive slope of the tangent line verifies the *n*-type nature of the material. An average of the intercept of the tangent line with the horizontal axis, at three different frequencies, resembles the flat band potential (E_{FB}) of the hematite films.[55,56] The E_{FB} values are applicable for estimating the conduction band of Fe_2O_3(110) and O_v_Fe_2O_3(110).[6] By assuming 0 $V_{Ag/AgCl}$ is equivalent to -4.64 eV_{vacuum}, the conduction band of Fe_2O_3(110) and O_v_Fe_2O_3(110) are determined to be -4.59 eV_{vacuum} and -4.51 eV_{vacuum}, respectively. With the aid of band gap values, obtained from the Tauc plot, the valence band was deduced which enable the construction of electronic structure of both samples as illustrated in Fig. 3(c). The estimated electronic structure is in agreement with the values reported previously.[57] The gradient of the tangent line was also utilized to compute the density of free charge carrier, N_D of the defect layer according to the following equation:

$$N_D = \frac{2}{e\varepsilon\varepsilon_0 A^2}\left[\frac{d\left(\frac{1}{C^2}\right)}{dE}\right]^{-1} \quad (1)$$

where e is charge of one electron, ε is dielectric constant of semiconductor, ε_0 is permittivity of free space, A is interfacial area of photoanode/electrolyte and $d(1/C^2)/dE$ is slope of the tangent line as determined in Mott-Schottky plot.[6] As expected, O_v_Fe_2O_3(110) possesses higher free carrier density (approximately 8.34×10^{19} cm^{-3}) than that of Fe_2O_3(110) (approximately 2.89×10^{19} cm^{-3}) which is primarily attributed to the excess of oxygen defective sites in the sample.

The increment of free carrier could be simply explained from the atomic arrangement in the crystal of hematite. Fig. 3(d-f) illustrates the primitive and hexagonal unit cells of a perfect hematite (α-Fe_2O_3) where the iron cation (Fe^{3+}) and oxygen anion (O^{2-}) are arranged in a corundum structure. In case of defective Fe_2O_3, the removal of one oxygen atom from the crystal lattice results in the generation of one point defect or so-called oxygen vacancies which simultaneously reduce the coordination number of the three neighboring iron ions. So, the electrons which are left behind, lead to the increment of total amount of majority carrier in Fe_2O_3 thin film. It is widely known that hematite is an *n*-type semiconductor,[58] where free electrons that form majority carrier in hematite, stemmed from the naturally existing oxygen vacancies. Nonetheless, fabrication of hematite in nitrogen environment amplifies the total number of oxygen vacancies which in turn considerably enhances the amount of free electrons. The higher carrier density can improve the conductivity of hematite which may eventually facilitate the charges separation.

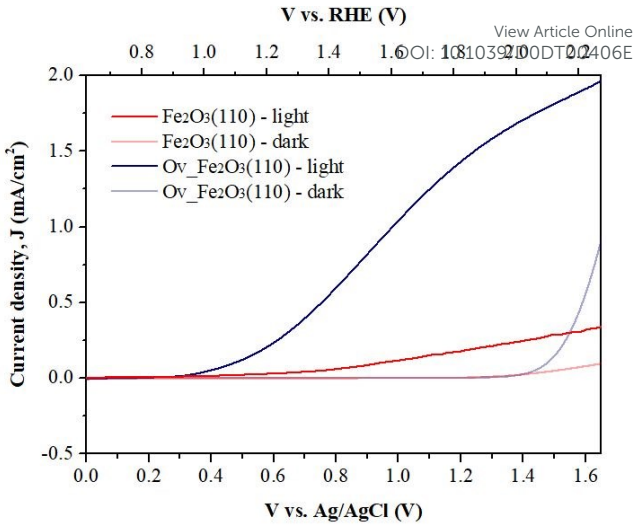

Fig. 4 Photoelectrochemical performance of Fe_2O_3(110) and O_v_Fe_2O_3(110) measured from front under simulated AM 1.5G solar irradiance (100 mW cm^{-2}) and dark condition.

The AACVD fabricated α-Fe_2O_3 films were tested in PEC cell as active photoanode and their performance were analyzed using linear sweep voltammetry (LSV). The current density vs. voltage curves of the samples are simulated by alternatively 1 Sun illumination followed by dark condition, as shown in Fig. 4. The current density of O_v_Fe_2O_3(110) sample is 1.49 mA cm^{-2} at potential of 1.23 $V_{Ag/AgCl}$ which is approximately 8 times higher than that of Fe_2O_3(110) (0.19 mA cm^{-2}). Obviously, oxygen vacancies are responsible for the substantial improvement of photocurrent generation. In addition, oxygen vacancies can also act as electron donors.[54] The PEC performance could be further boost by employing co-catalyst or introducing surface passivation layer which is beyond the scope of this study. However, taking into account the rapid fabrication process and outstanding performance improvement achieved in this work, defective hematite photoanode obtained using AACVD technique could serve as a leaping stone towards the commercialization of PEC technology.

In order to gain a deeper insight into the effects of oxygen vacancies towards the photocatalytic activity of hematite, the electrical properties of the thin film was further scrutinized. Charge transfer kinetics at the interfaces is one of the main factor which determines the PEC performance of a photoanode.[59] To evaluate this effect, electrochemical impedance spectroscopy (EIS) was carried out using similar cell configuration as that of LSV analysis, under light illumination at bias voltage of 1.2 $V_{Ag/AgCl}$. The experimental data were best fitted using Voigt circuit comprising of an R component connected in series with two R-Q parallel components as illustrated by the equivalent circuit in the bottom inset of

View Article Online
DOI: 10.1039/D0DT00406E

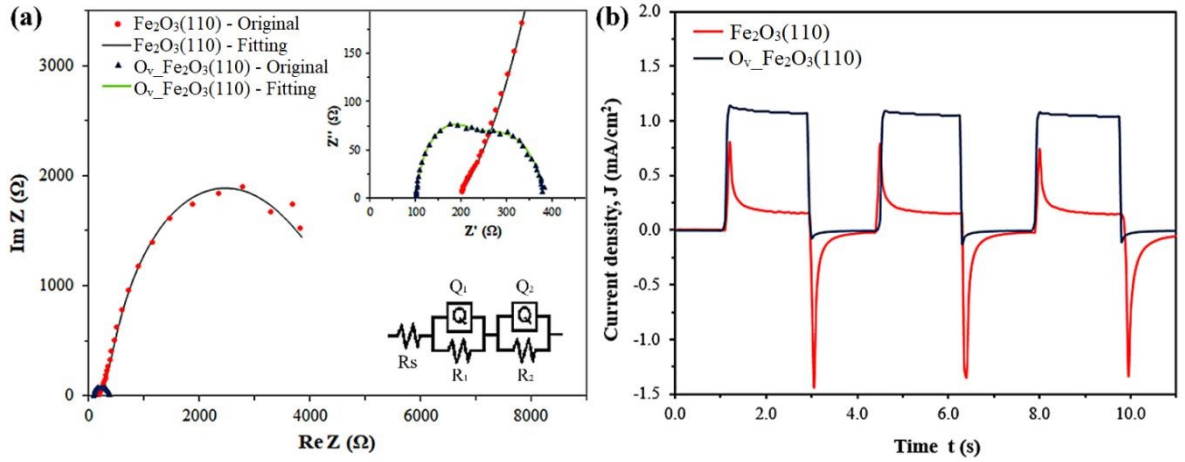

Fig. 5 (a) Nyquist plot of electrochemical impedance spectroscopy. Top and bottom inset are the zoom-in view and equivalent circuit for fitting the experimental data, respectively. (b) Current density-time graph of the corresponding samples measured at 1.2 $V_{Ag/AgCl}$.

Table 1. Fitted resistance of EIS, free carrier density and transient time of Fe_2O_3(110) and O_v_Fe_2O_3(110).

Sample	R_S (Ω)	R_1 (Ω)	R_2 (Ω)	N_D (cm^{-3})	*Transient time (s)*
Fe_2O_3(110)	194.6	3039	6307	2.89×10^{19}	0.08
O_v_Fe_2O_3(110)	101.4	120.7	162	8.34×10^{19}	0.38

Nyquist plot (Fig. 5(a)). Both R-Q parallel components correspond to the two imperfect semicircles observed in the fitted line. R_1-Q_1 component (i.e. the semicircle at high frequency domain) can be attributed to the charge transport process within the bulk of hematite film whereas R_2-C_2 component (i.e. the semicircle at low frequency domain) can be attributed to the charge transfer process at the electrolyte/hematite photoanode interface. As evident from Table 1, O_v_Fe_2O_3(110) sample shows smaller semicircles than that of Fe_2O_3(110), which has much lower charge transport transfer in the bulk (R_1) and charge transfer resistance at the interface (R_2). In other words, injection rate of holes at the surface of O_v_Fe_2O_3(110) into the electrolyte is relatively high, expediting the oxidation process of water molecules to oxygen. Meanwhile, low charge transport resistance within the bulk of O_v_Fe_2O_3(110) film allows rapid transport of the photoexcited electrons towards counter electrode for hydrogen production.

The chopping current-time (I-t) curve in Fig. 5(b) indicates that the sample is highly responsive towards the presence and absence of light. The curve was then converted to ln D vs. time graph (Fig. S3) using equation S2-S3 of the Supporting Information, to determine the transient time where longer transient time corresponds to slower charge recombination rate and vice versa.[60] As listed in Table 1, the values were estimated to be 0.08 and 0.38 sec for Fe_2O_3(110) and O_v_Fe_2O_3(110), respectively, implying that oxygen vacancies retard charge recombination process and increase the electron lifetime. The stability of O_v_Fe_2O_3(110) under prolonged exposure towards light and bias voltage was also examined. As can be seen from Fig. S4, O_v_Fe_2O_3(110) sample exhibits relatively stable performance at constant light illumination for a duration of 30 min at a bias voltage of 1.2 $V_{Ag/AgCl}$. This finding proves that high density of oxygen vacancies in hematite does not adversely affect the stability of the photoanode against light soaking or electrical bias. The reliability of the analysis and the reproducibility of the hematite thin film was verified by measuring the performance of several samples fabricated under identical condition. Fig. S5 shows the photocurrent density of four Fe_2O_3(110) and O_v_Fe_2O_3(110) photoanodes prepared using AACVD technique. As compared to the LSV result discussed earlier, consistent results were observed for the photocurrent density which proves that the maximum PEC performance is actually achievable using 10 min deposition period in nitrogen environment.

Based on the analysis above, the significant increase of PEC performance for hematite film fabricated under pure nitrogen flow in relative to that sample prepared using purified air can be ascribed to several factors. For the most part, greater density of oxygen vacancies is the most influential factor that foster the photocurrent generation of O_v_Fe_2O_3(110). Oxygen vacancies increase the conductivity of the bulk hematite, leading to better charge separation and prevent charge recombination.[61] This is supported by the low charge transport resistance and longer transient time as determined from EIS and chopping I-t analysis, respectively. Meanwhile, the reduced charge transfer resistance at the interface as determined by EIS was also contributed to the presence of oxygen vacancies. The defect sites facilitate the adsorption of water molecules on the surface of hematite which subsequently accelerate the electrocatalytic process. In addition, the presence of oxygen vacancies contributes to the improvement of light absorption capability of the O_v_Fe_2O_3(110) sample as detected by UV-Vis spectroscopy. The stronger light absorption intensifies the number of photoexcited electron-hole pairs which ultimately increase the total amount of charges available for oxidation process of water. From the viewpoint of crystal structure, (110) plane provide a high-mobility pathway for photoexcited electrons

whereas (104) plane is favorable for trapping the generated holes at the surface of hematite, rendering the holes available for oxygen evolution reaction (OER). Recently, it has been reported that (012) facet has optimal interaction with all oxygenated intermediates which is beneficial for intermediary adsorption/desorption and hence decrease the kinetics barrier for OER. The balance between these crystal planes that was observed in XRD pattern of O_v_Fe_2O_3(110) sample promotes charge transport and charge separation which eventually increase the photocurrent.

On the other hand, the morphological properties of Fe_2O_3(110) sample with nanoflakes structure are in fact superior to O_v_Fe_2O_3(110) with shard-like shapes. As shown in FESEM and AFM analyses, the thin structure of nanoflakes could shorten the path length for electron and hole transport which may prevent charge recombination process induced by the limited charge carrier diffusion length. Besides, rougher surface of nanoflakes would also enlarge the available sites for photocatalytic activity escalating the charge separation efficiency. In spite of that, Fe_2O_3(110) still exhibited much lower current density in comparison to O_v_Fe_2O_3(110) suggesting that film morphology has less influence towards the PEC performance. Thus, we believe that point defects related to oxygen vacancies is the paramount features contributing to the extraordinary generation of photocurrent density.

To validate that oxygen vacancies is the predominant parameter governing the efficiency of Fe_2O_3 in this study, the effect of thickness and surface roughness of the samples fabricated under different gas flow were further investigated. Firstly, the deposition period for Fe_2O_3(110) and O_v_Fe_2O_3(110) samples was manipulated with the aim to control the film thickness where longer deposition time would lead to greater thickness and vice versa. Duration of 10, 20, 40 and 60 min was selected for the fabrication of Fe_2O_3(110) whereas 5, 10, 15 and 20 min was selected for O_v_Fe_2O_3(110). The time of deposition was chosen differently to achieve the optimum PEC performance for the respective devices. As observed in LSV analysis (Fig. 6), the performance of hematite samples fabricated either via purified air or pure nitrogen flow improves with deposition period until a certain optimum value and then followed by significant performance drop. The champion device for the Fe_2O_3(110) group was shown by sample prepared for 40

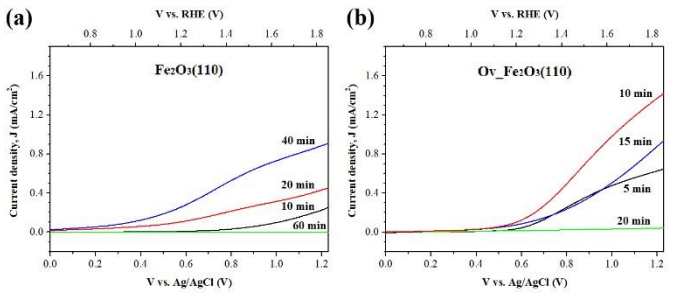

Fig. 6 PEC performance of (a) Fe_2O_3(110) and (b) O_v_Fe_2O_3(110) fabricated using AACVD at diverse deposition time.

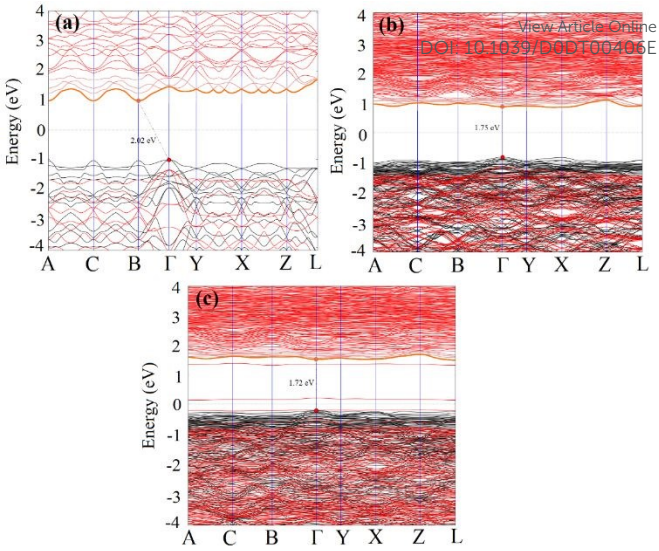

Fig. 7 Band structure of (a) bulk Fe_2O_3, (b) Fe_2O_3(110) and (c) O_v_Fe_2O_3(110).

min whereas only 10 min deposition time is needed to reach the optimum condition for the O_v_Fe_2O_3(110) group. Even though the best O_v_Fe_2O_3(110) photoanode has shorter deposition time which resulted in thinner layer, the PEC performance is much better than thicker Fe_2O_3(110) counterpart signifying that the photoelectrocatalytic activity of hematite heavily depends on the oxygen vacancies.

Surface roughness of all Fe_2O_3(110) samples was examined as shown in Fig. S6. As expected, prolonging the deposition time of Fe_2O_3(110) up to 40 min lead to gradual increment in the RMS roughness due to the conversion of nanoflakes to nanoflowers (Fig. S7). The roughness of the best sample in Fe_2O_3(110) group exhibits much higher value (129.6 nm) compared to that roughness of the optimum O_v_Fe_2O_3(110) (49.5 nm) as seen in Fig. 1(f). Previous reports have witnessed notable enhancement in the generated PEC photocurrent upon increasing the roughness of photoanode since rougher surface enlarges the available sites for catalytic activity. In spite of this well-known fact, O_v_Fe_2O_3(110) fabricated for 10 min which possesses relatively lower RMS roughness with respect to Fe_2O_3(110) fabricated for 40 min still exhibits higher PEC performance indicative to greater impact of oxygen vacancies towards water oxidation process.

It is noted that the optimum O_v_Fe_2O_3(110) sample is unable to be as thick as Fe_2O_3(110) in spite of the fact that thicker layer may increase light absorption. Basically, an increase in the hematite film thickness produces a corresponding increase in light absorption of the film. This results in higher excitation rate

View Article Online
DOI: 10.1039/D0DT00406E

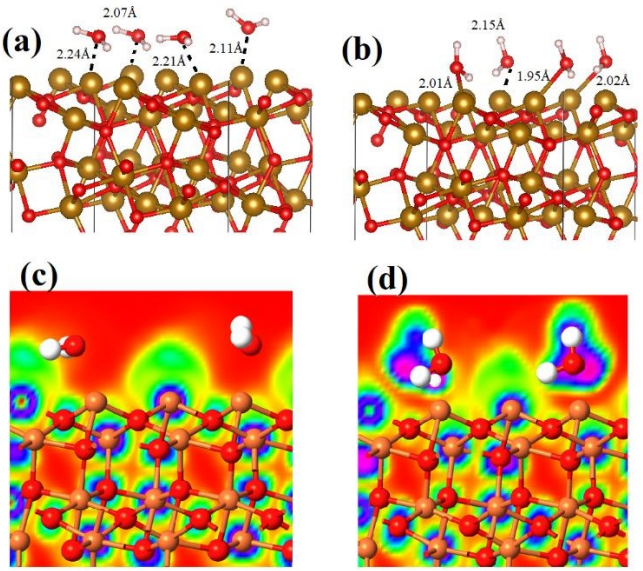

Fig. 8 Optimized structures of (a) $Fe_2O_3(110)@H_2O$, (b) $O_v\_Fe_2O_3(110)@H_2O$, electron localization function map of (c) $Fe_2O_3(110)@H_2O$, and (d) $O_v\_Fe_2O_3(110)@H_2O$.

of electron-hole pairs and greater hydrogen production. However, extremely thick hematite film substantially lowers the overall performance owing to the limitation of charge carrier diffusion length. Nonetheless, in the case of $O_v\_Fe_2O_3(110)$ which possesses high amount of oxygen vacancies, the oxygen vacancies can create trap states at the surface of hematite layer which subsequently making the photoanode to behave like an insulator. In other words, extremely large quantities of oxygen defect sites would reduce the charge transfer ability at the photoanode/electrolyte interface, intensify charge recombination rate and plummet the generation of current density. Besides, several studies previously have proven that oxygen vacancies are able to migrate to the surface of oxide-based semiconductor such as TiO_2 under electrical bias, which might be applicable for hematite photoanode.[62] If this is the case, this feature would be detrimental for hematite film with high concentration of oxygen vacancies, since hematite requires relatively large overpotential (about 0.5-0.6 V) to drive the superior charge transport, charge separation and charge transfer efficiency provided by oxygen vacancies while preserving high light absorption ability of the film. To give a more comprehensive view regarding this phenomenon, deeper analysis is still ongoing in our lab which will be discussed in a separate report.

Electronic properties

In order to countercheck our experimental data, DFT simulations have been carried for the pristine $Fe_2O_3(110)$ and its oxygen defective specie such as $O_v\_Fe_2O_3(110)$. Using spin-polarized DFT simulations, a band gap of 2.02 eV is obtained for the bulk hematite while it reduces to 1.75 eV in case of [110] terminated Fe_2O_3 as shown in Table 2. On making 2% oxygen deficient, the electronic and catalytic properties further improve. The Fermi energy level increases from 6.17 to 6.78 eV while the band gap reduces to 1.72 eV. This data nicely correlates our experimental results. Comparative analysis of the data of Table 2 led us to conclude that charge carrier mobilities of $O_v\_Fe_2O_3(110)$ are better than that of their pristine counterpart. The reason behind this is, oxygen vacancy produces flat bands between VBM and CBM as can be seen from Fig. 7. These flat bands are responsible as hole trapping centers, which alternatively reduce the rate of electron hole recombination. Again, this statement is also consistent with our experimental data and the already reported similar theoretical reports.[63]

Moreover, the photocatalytic activity of these two surfaces are investigated from the water molecules adsorption energies. Four water molecules are adsorbed over the surfaces of $Fe_2O_3(110)$ and $O_v\_Fe_2O_3(110)$ at appropriate distance and then allowed to relax. Optimized structures of $Fe_2O_3(110)@H_2O$ and $O_v\_Fe_2O_3(110)@H_2O$ systems along with their electrostatic potential maps are given in Fig. 8, where the O atoms of water has strong inter-bonding with the surface Fe atoms of $O_v\_Fe_2O_3(110)@H_2O$ system, compared to that of pristine $O_v\_Fe_2O_3(110)@H_2O$ system.

The stronger the O—Fe bonding, the higher will be the water splitting ability. As we can see from Fig. 8, the average O—Fe bondings in $Fe_2O_3(110)@H_2O$ is about 2.16 Å while it is about 2.03 Å in $O_v\_Fe_2O_3(110)@H_2O$. Consequently, these short inter-bondings are responsible for strong water adsorption energy. The per water molecule adsorption energy of $Fe_2O_3(110)@H_2O$ and $O_v\_Fe_2O_3(110)@H_2O$ along with their surface formation energies are listed in Table 3. The surface of pristine $Fe_2O_3(110)$ is comparatively stable, having surface formation energy of 0.48 eV/Å^2 while that of oxygen deficient one is about 0.44 eV/Å^2. On

Table 2: DFT simulated Fermi energy level, VBM, CBM, Band Gap, and Effective Masses of Photogenerated Electrons and Holes. Effective masses of electrons and holes are estimated from the Calculated Band Structure of CBM and VBM, respectively.

Species	*Fermi Energy*	*Direction in Brillouin zone*	m_e^*/m_0 (m_e)	m_h^*/m_0 (m_e)	*VB (eV)*	*CB (eV)*	*Band gap (eV)*
Bulk Fe_2O_3	-6.13	G→B	0.03	0.09	-7.16	-5.14	2.02
$Fe_2O_3(110)$	-6.17	G→G	6.13	10.0	-7.03	-5.28	1.75
$O_v\_Fe_2O_3(110)$	-6.78	G→G	4.01	1.32	-6.97	-5.25	1.72

View Article Online
DOI: 10.1039/D0DT04055F

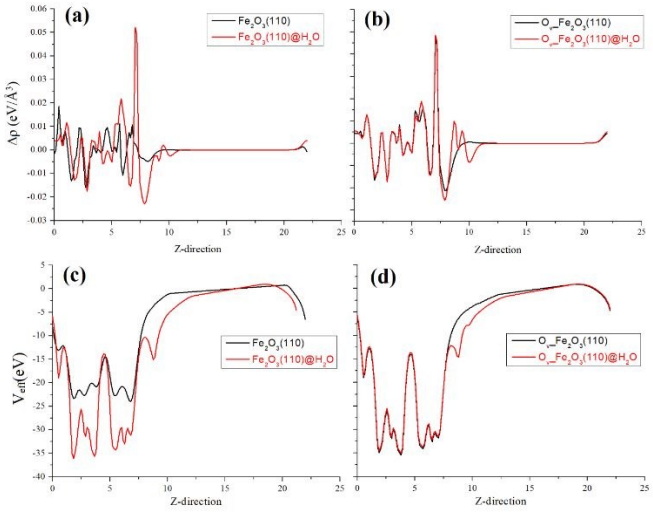

Fig. 9 EDD plot of (a) Fe_2O_3(110), (b) O_v_Fe_2O_3(110), Effective potentials plot of (c) pristine Fe_2O_3(110) and (d) oxygen defective surfaces along z-direction; with and without water molecules.

the other hand, the O_v_Fe_2O_3(110) is more active which is responsible for higher per water molecule adsorption such as -63.44 kJ/mol. This high water adsorption energy can be correlated to experimental lower overpotential of water splitting. In summary, oxygen defective O_v_Fe_2O_3(110) has higher catalytic activity (in term of strong water adsorption energy) to that of pristine Fe_2O_3(110). Again, these results and discussion strongly corroborate our experimental data.

In addition, we also calculated the electron difference densities of Fe_2O_3(110) and O_v_Fe_2O_3(110) with and without water molecule's interactions, as shown in Fig. 9. From Fig. 9a, it can be inferred that electrons are donated from water molecules toward Fe_2O_3(110) and results an overall stable nucleophilic species. This can be seen from the red line of Fig. 9a, in the range of 7.5 to 10 Å along z-axes. On the other hand, the interaction of water molecules with that of O_v_Fe_2O_3(110) surface is totally opposite. The O_v_Fe_2O_3(110) is became more electro-positive, upon interaction with water which form O_v_Fe_2O_3(110)@H_2O system. From Fig. 9b, it can be easily seen (red line in the range of 8 to 10.5 Å along z-direction) that water molecules have donated electronic cloud density to O_v_Fe_2O_3(110), in the positive scale.

Finally, we also simulated the average effective potentials of these surfaces along z-direction, with and without water molecules which are given in Fig. 9c and d. Results and discussion of theses effective potential plots led us to conclude that both Fe_2O_3(110) and O_v_Fe_2O_3(110) are stable surface with and without water interaction, however, O_v_Fe_2O_3(110) is more active compared to pristine Fe_2O_3(110).

Table 3. Formation energy (eV/Å²) and adsorption energy (kJ/mol) per water molecule over the pristine and oxygen defective surface of hematite.

Species	*Formation Energy (eV/Å²)*	E_{ad}
Fe_2O_3(110)	0.48	-
Fe_2O_3(110)@H_2O	-	-56.93
O_v_Fe_2O_3(110)	0.44	-
O_v_Fe_2O_3(110)@H_2O	-	-63.44

Conclusions

In summary, we have successfully developed defective hematite thin films in a very short timescale through AACVD technique, simply by deploying pure nitrogen flow during the fabrication process. Photocurrent generation of the hematite films prepared under nitrogen environment exhibited drastic improvement of about 8 times in comparison to purified air-based samples mainly due to the formation of higher density of oxygen vacancies. The point defects associated with oxygen vacancies improves the bulk conductivity of hematite enabling fast charge transport and efficient charge separation. While recombination rate of electron-hole pairs decreased as proven from the increase of transient time, oxygen vacancies also encouraged hole transfer process at the surface of hematite photoanode which expedite water oxidation reaction. Nonetheless, proper control of thickness is necessary to avoid undesirable charge recombination as a consequence of trap states formation. The best PEC performance was obtained for hematite film prepared for merely 10 min in nitrogen environment using AACVD technique. In order to countercheck and confirm our experimental data, DFT simulations are carried out for the pristine and oxygen defective α-Fe_2O_3 thin films. We observed that oxygen defective hematite has a narrow band gap, electron-hole trapped center in the band structure, and strong adsorption energy for water molecules compared to that of pristine hematite. The development of rapid fabrication process for the production of the film could pave the way for realizing successful commercialization of this green technology.

Conflicts of interest

There are no conflicts to declare.

Acknowledgements

The authors would like to express their gratitude to Universiti Kebangsaan Malaysia for the financial aid through grant DIP-2018-009.

References

1 M. F. Mohamad Noh, N. A. Arzaee, I. N. Nawas Mumthas, N. A. Mohamed, S. N. F. Mohd Nasir, J. Safaei, A. R. bin M. Yusoff, M. K. Nazeeruddin and M. A. Mat Teridi, *J. Mater. Chem. A*, 2020, **8**, 10481–10518.

2 M.-I. Jamesh and X. Sun, *J. Power Sources*, 2018, **400**, 31–68.

3 Z. Wang, C. Li and K. Domen, *Chem. Soc. Rev.*, 2019, **48**, 2109–2125.

4 L. Wang, Y. Wang, P. Schmuki, S. Kment and R. Zboril,

Electrochim. Acta, 2018, **260**, 212–220.
5 M. F. Mohamad Noh, M. F. Soh, M. A. Riza, J. Safaei, S. N. F. Mohd Nasir, N. W. Mohamad Sapian, C. H. Teh, M. A. Ibrahim, N. Ahmad Ludin and M. A. Mat Teridi, *Phys. Status Solidi*, 2018, **255**, 1700570.
6 M. F. M. Noh, M. F. Soh, C. H. Teh, E. L. Lim, C. C. Yap, M. A. Ibrahim, N. A. Ludin and M. A. M. Teridi, *Sol. Energy*, 2017, **158**, 474–482.
7 J. Safaei, H. Ullah, N. A. Mohamed, M. F. Mohamad Noh, M. F. Soh, A. A. Tahir, N. Ahmad Ludin, M. A. Ibrahim, W. N. R. Wan Isahak and M. A. Mat Teridi, *Appl. Catal. B Environ.*, 2018, **234**, 296–310.
8 N. A. Mohamed, J. Safaei, A. F. Ismail, M. N. Khalid, M. F. A. Mohd Jailani, M. F. M. Noh, N. A. Arzaee, D. Zhou, J. S. Sagu and M. A. M. Teridi, *Mater. Res. Bull.*, 2020, **125**, 110779.
9 N. A. Mohamed, J. Safaei, A. F. Ismail, M. F. Mohamad Noh, N. A. Arzaee, N. N. Mansor, M. A. Ibrahim, N. A. Ludin, J. S. Sagu and M. A. Mat Teridi, *J. Alloys Compd.*, 2019, **818**, 152916.
10 J. Safaei, N. A. Mohamed, M. F. Mohamad Noh, M. F. Soh, N. A. Ludin, M. A. Ibrahim, W. N. Roslam Wan Isahak and M. A. Mat Teridi, *J. Mater. Chem. A*, 2018, **6**, 22346–22380.
11 N. Dzade, A. Roldan and N. de Leeuw, *Minerals*, 2014, **4**, 89–115.
12 A. G. Tamirat, J. Rick, A. A. Dubale, W.-N. Su and B.-J. Hwang, *Nanoscale Horizons*, 2016, **1**, 243–267.
13 S. J. A. Moniz, S. A. Shevlin, D. J. Martin, Z.-X. Guo and J. Tang, *Energy Environ. Sci.*, 2015, **8**, 731–759.
14 J. Joy, J. Mathew and S. C. George, *Int. J. Hydrogen Energy*, 2018, **43**, 4804–4817.
15 Y. Zhang, S. Jiang, W. Song, P. Zhou, H. Ji, W. Ma, W. Hao, C. Chen and J. Zhao, *Energy Environ. Sci.*, 2015, **8**, 1231–1236.
16 C. Zhu, C. Li, M. Zheng and J. Delaunay, *ACS Appl. Mater. Interfaces*, 2015, **7**, 22355–22363.
17 K. Sivula, R. Zboril, F. Le Formal, R. Robert, A. Weidenkaff, J. Tucek, J. Frydrych and M. Grätzel, *J. Am. Chem. Soc.*, 2010, **132**, 7436–7444.
18 M. Li, Y. Qiu, W. Qiu, S. Tang, S. Xiao, S. Ma, G. Ouyang, Y. Tong and S. Yang, *ACS Appl. Energy Mater.*, 2018, **1**, 5836–5841.
19 S. Kment, F. Riboni, S. Pausova, L. Wang, L. Wang, H. Han, Z. Hubicka, J. Krysa, P. Schmuki and R. Zboril, *Chem. Soc. Rev.*, 2017, **46**, 3716–3769.
20 N. A. Arzaee, M. F. Mohamad Noh, A. Ab Halim, M. A. F. Abdul Rahim, N. A. Mohamed, J. Safaei, A. Aadenan, S. N. Syed Nasir, A. F. Ismail and M. A. Mat Teridi, *Ceram. Int.*, 2019, **45**, 16797–16802.
21 A. G. Hufnagel, H. Hajiyani, S. Zhang, T. Li, O. Kasian, B. Gault, B. Breitbach, T. Bein, D. Fattakhova-Rohlfing, C. Scheu and R. Pentcheva, *Adv. Funct. Mater.*, 2018, **28**, 1804472.
22 S. Li, J. Cai, Y. Liu, M. Gao, F. Cao and G. Qin, *Sol. Energy Mater. Sol. Cells*, 2018, **179**, 328–333.
23 X. Chai, H. Zhang, Q. Pan, J. Bian, Z. Chen and C. Cheng, *Appl. Surf. Sci.*, 2019, **470**, 668–676.
24 R. Rajendran, Z. Yaakob, M. A. Mat Teridi, M. S. Abd Rahaman and K. Sopian, *Mater. Lett.*, 2014, **133**, 123–126.
25 L. Wang, K. Marcus, X. Huang, Z. Shen, Y. Yang and Y. Bi, *Small*, 2018, **14**, 1704464.
26 T.-Y. Yang, H.-Y. Kang, U. Sim, Y.-J. Lee, J.-H. Lee, B. Koo, K. T. Nam and Y.-C. Joo, *Phys. Chem. Chem. Phys.*, 2013, **15**, 2117.
27 X. Zhao, J. Feng, S. Chen, Y. Huang, T. C. Sum and Z. Chen, *Phys. Chem. Chem. Phys.*, 2017, **19**, 1074–1082.
28 Z. Wang, X. Mao, P. Chen, M. Xiao, S. A. Monny, S. Wang, M. Konarova, A. Du and L. Wang, *Angew. Chemie*, 2019, **131**, 1042–1046.
29 S. D. Ponja, B. A. D. Williamson, S. Sathasivam, D. O. Scanlon, I. P. Parkin and C. J. Carmalt, *J. Mater. Chem. C*, 2018, **6**, 7257–7266.
30 R. Naeem, M. A. Ehsan, A. Rehman, Z. H. Yamani, A. S. Hakeem and M. Mazhar, *New J. Chem.*, 2018, **42**, 5256–5266.
31 A. A. Tahir, M. A. Mat-Teridi and K. G. U. Wijayantha, *Phys. status solidi - Rapid Res. Lett.*, 2014, **8**, 976–981.
32 S. N. F. M. Nasir, H. Ullah, M. Ebadi, A. A. Tahir, J. S. Sagu and M. A. Mat Teridi, *J. Phys. Chem. C*, 2017, **121**, 6218–6228.
33 H. Alessa, M. F. M. Noh, I. N. N. Mumthas, K. G. U. Wijayantha and M. A. M. Teridi, *Phys. status solidi*, 2020, **217**, 1900607.
34 M. F. Mohamad Noh, N. A. Arzaee, J. Safaei, N. A. Mohamed, H. P. Kim, A. R. Mohd Yusoff, J. Jang and M. A. Mat Teridi, *J. Alloys Compd.*, 2019, **773**, 997–1008.
35 AtomistixToolKit version 2017.1, QuantumWise A/S (www.quantumwise.com).
36 VirtualNanoLab version 2017.1, QuantumWise A/S (www.quantumwise.com).
37 G. Kresse and D. Joubert, *Phys. Rev. B*, 1999, **59**, 1758–1775.
38 K. Persson, Materials Data on Fe2O3 (SG:167) by Materials Project. United States: N. p., 2014. Web.
39 A. J. Tkalych, K. Yu and E. A. Carter, *J. Phys. Chem. C*, 2015, **119**, 24315–24322.
40 H. Ullah, A. A. Tahir, S. Bibi, T. K. Mallick and S. Z. Karazhanov, *Appl. Catal. B Environ.*, 2018, **229**, 24–31.
41 H. Ullah, A. A. Tahir and T. K. Mallick, *Appl. Catal. B Environ.*, 2018, **224**, 895–903.
42 J. Enkovaara, C. Rostgaard, J. J. Mortensen, J. Chen, M. Dułak, L. Ferrighi, J. Gavnholt, C. Glinsvad, V. Haikola, H. A. Hansen, H. H. Kristoffersen, M. Kuisma, A. H. Larsen, L. Lehtovaara, M. Ljungberg, O. Lopez-Acevedo, P. G. Moses, J. Ojanen, T. Olsen, V. Petzold, N. A. Romero, J. Stausholm-Møller, M. Strange, G. A. Tritsaris, M. Vanin, M. Walter, B. Hammer, H. Häkkinen, G. K. H. Madsen, R. M. Nieminen, J. K. Nørskov, M. Puska, T. T. Rantala, J. Schiøtz, K. S. Thygesen and K. W. Jacobsen, *J. Phys. Condens. Matter*, 2010, **22**, 253202.
43 S. He, C. Yan, X.-Z. Chen, Z. Wang, T. Ouyang, M.-L. Guo and Z.-Q. Liu, *Appl. Catal. B Environ.*, 2020, **276**, 119138.
44 Y. Makimizu, N. T. Nguyen, J. Tucek, H. Ahn, J. Yoo, M. Poornajar, I. Hwang, S. Kment and P. Schmuki, *Chem. – A Eur. J.*, 2020, **26**, 2685–2692.

View Article Online
DOI: 10.1039/D0DT00406E

45 Y. Makimizu, J. Yoo, M. Poornajar, N. T. Nguyen, H.-J. Ahn, I. Hwang, S. Kment and P. Schmuki, *J. Mater. Chem. A*, 2020, **8**, 1315–1325.

46 Z. Wang, X. Mao, P. Chen, M. Xiao, S. A. Monny, S. Wang, M. Konarova, A. Du and L. Wang, *Angew. Chemie Int. Ed.*, 2019, **58**, 1030–1034.

47 R. Morrish, M. Rahman, J. M. D. MacElroy and C. A. Wolden, *ChemSusChem*, 2011, **4**, 474–479.

48 J. Wu, P. Huang, H. Fan, G. Wang and W. Liu, *ACS Appl. Mater. Interfaces*, 2020, **12**, 30304–30312.

49 Y. Fu, Y.-R. Lu, F. Ren, Z. Xing, J. Chen, P. Guo, W.-F. Pong, C.-L. Dong, L. Zhao and S. Shen, *Sol. RRL*, 2020, **4**, 1900349.

50 B. Jansi Rani, G. Ravi, R. Yuvakkumar, S. Ravichandran, F. Ameen and S. AlNadhary, *Renew. Energy*, 2019, **133**, 566–574.

51 X. Bu, Y. Gao, S. Zhang and Y. Tian, *Chem. Eng. J.*, 2019, **355**, 910–919.

52 Z. Zhou, J. Liu, R. Long, L. Li, L. Guo and O. V. Prezhdo, *J. Am. Chem. Soc.*, 2017, **139**, 6707–6717.

53 J. Lee and S. Han, *Phys. Chem. Chem. Phys.*, 2013, **15**, 18906.

54 J. Li, S. K. Cushing, P. Zheng, F. Meng, D. Chu and N. Wu, *Nat. Commun.*, 2013, **4**, 2651.

55 X. Shi, L. Cai, M. Ma, X. Zheng and J. H. Park, *ChemSusChem*, 2015, **8**, 3192–3203.

56 K. C. Leonard, K. M. Nam, H. C. Lee, S. H. Kang, H. S. Park and A. J. Bard, *J. Phys. Chem. C*, 2013, **117**, 15901–15910.

57 M. F. Mohamad Noh, C. H. Teh, R. Daik, E. L. Lim, C. C. Yap, M. A. Ibrahim, N. Ahmad Ludin, A. R. bin Mohd Yusoff, J. Jang and M. A. Mat Teridi, *J. Mater. Chem. C*, 2018, **6**, 682–712.

58 C. Li, Z. Luo, T. Wang and J. Gong, *Adv. Mater.*, 2018, **30**, 1707502.

59 N. A. Mohamed, H. Ullah, J. Safaei, A. F. Ismail, M. F. Mohamad Noh, M. F. Soh, M. A. Ibrahim, N. A. Ludin and M. A. Mat Teridi, *J. Phys. Chem. C*, 2019, **123**, 9013–9026.

60 A. A. S. M. Radzi, J. Safaei and M. A. M. Teridi, *Nano-Structures & Nano-Objects*, 2019, **18**, 100274.

61 J. H. Kim, Y. J. Jang, J. H. Kim, J.-W. Jang, S. H. Choi and J. S. Lee, *Nanoscale*, 2015, **7**, 19144–19151.

62 M. F. M. Noh, N. A. Arzaee and M. A. M. Teridi, in *Solar Cells*, eds. S. K. Sharma and K. Ali, Springer International Publishing, Cham, 2020, pp. 283–305.

63 M. d'Avezac, M. Calandra and F. Mauri, *Phys. Rev. B*, 2005, **71**, 205210.

Graphical Abstract

View Article Online
DOI: 10.1039/D0DT00406E

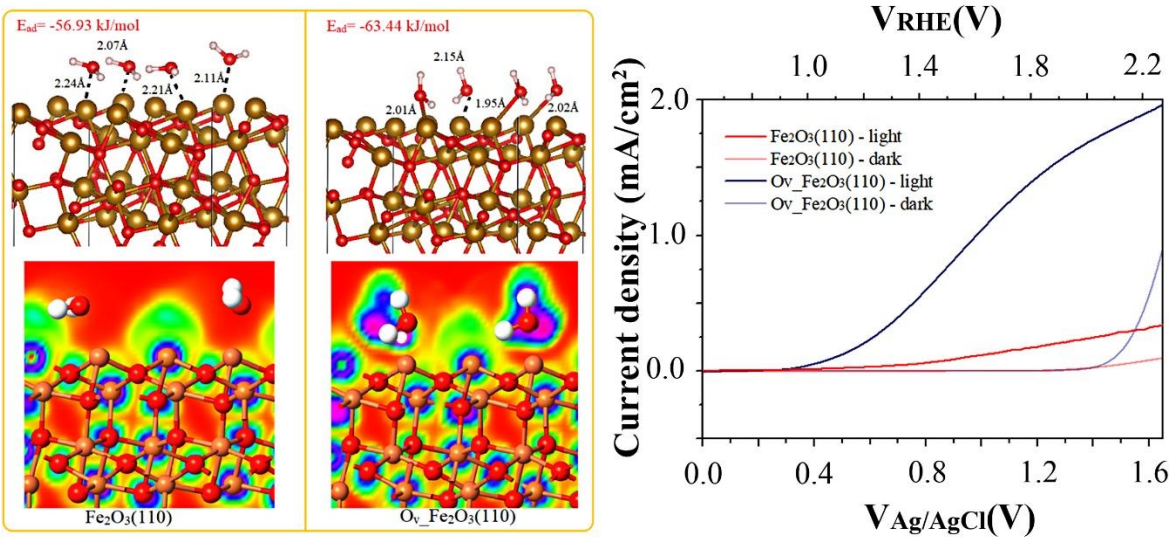

Oxygen vacancies boost the photoelectrochemical water splitting reaction of hematite photoanode having (110) dominant crystal plane.